materials

MDPI

Article

Alumina ceramics for armor protection via 3D printing with designed slurry

Dongjiang Zhang [1,2], Zhengang Cui [1,*], Xin Chen [3], Chunxu Pang [2], Xuncheng Guo [2], Xiqing Xu [3,*]

[1] Shenyang Ligong University, Shenyang 110159, China;
[2] Xi'an Modern Control Technology Research Institute, Xi'an 710065,China;
[3] Chang'an University, Xi'an 710061, China;
* Corresponding author, Email: cuizg024@163.com (Z.C.); xiqingxu@chd.edu.cn (X.X.)

Abstract: Alumina ceramic is an ideal candidate for armor protection, but limited by the difficult molding or machining processing. 3D printing displays superior geometric flexibility, and shows well potential in the preparation of ceramic ceramics for armor protection. In this work, alumina ceramics were manufactured by 3D printing, and the effects of different monomers on the photosensitive slurry and sintered ceramics were investigated. The photosensitive slurries using dipropylene glycol diacrylate (DPGDA) as monomers displayed optimal curing performance with low viscosity, small volume shrinkage and low critical exposure energy, and each of the above properties was conducive to the curing performance in 3D printing, making it a suitable formula for 3D printing of ceramic materials. In the 3D printed ceramics with DPGDA as monomer, dense and uniform microstructure was exhibited after sintering without anisotropic features. In comparison, the sample with trimethylolpropane triacrylate (TMPTA) showed anisotropic microstructure with serious interlayer gaps and numerous pores. Attributed to the dense uniform microstructure, the sample with DPGDA exhibited superior mechanical properties, including Vickers hardness of 19.8±1.6 GPa, fracture toughness of 2.6±0.27 MPa·m$^{1/2}$, bending strength of 690±54 MPa, and dynamic strength of 3.7 GPa at strain rate of 1200 s^{-1}, which was beneficial to the application in armor protection.

Keywords: alumina ceramics; 3D printing; monomer; interlayer gap; dynamic mechanical property.

Citation: To be added by editorial staff during production.

Academic Editor: Firstname Lastname

Received: date
Accepted: date
Published: date

1. Introduction

Alumina ceramic is one of the most important ceramics in the fileds of aerospace, machinery, metallurgy, semiconductors and armor protection [1-5], attributed to their advantages in hardness, wear resistance, high-temperature stability, chemical corrosion resistance [6-8]. For instance, serving as armor protective materials, alumina ceramics with lightweight turn to counteract the high-speed ammunition by virtue of the high hardness and high strength at high strain rates [9]. However, special shapes are generally required in armor protection systems, and armor protection ceramics with high strength and hardness must be processed using diamond grinding tools [10-12], and the expensive cost of machining processing reaches about 80% of the total cost. In addition, molds are demanded in the manufacture of complex-shaped ceramic components, which results in low forming accuracy and low efficiency.

3D printing [13-15], i.e., additive manufacturing technology, displays superior geometric flexibility, high precision, and high efficiency, making making it a suitable molding method for ceramic materials with complex shapes. By virtue of 3D printing technology, ceramic materials have achieved a huge leap in geometric flexibility, and the production of ceramics with special shapes becomes easier, which highly promotes the development

of complex-shaped ceramic armor materials [16, 17]. There are various kinds of 3D printing technologies for ceramic materials, including ink-jet printing, fused deposition modeling, selective laser sintering, digital light processing, and stereo lithography[18-20], among which digital light processing (DLP) 3D printing [21-23] is widely used in ceramic materials due to the high printing accuracy and fast forming speed.

The DLP 3D printing relies on a curing reaction of the photosensitive resin into polymers under the irradiation of UV light, after which the ceramic powder is bonded into a green body with certain strength and smooth surface. Photosensitive resins [24, 25] are mainly composed of oligomers, monomers, photoinitiators, dispersants, and other additives. Monomers undergo polymerization reactions with the excitation of photoinitiators under UV irradiation, and the type of monomer directly affects the 3D printing performance of photosensitive resins, as well as the structure and properties of 3D printed ceramic materials. According to the Krieger Douberty model [26], the viscosity of ceramic slurries is positively correlated with the viscosity of photosensitive resins. Therefore, monomers in low viscosity should be selected to obtain ceramic slurries with high solid content and low viscosity to meet the requirement for 3D printing [27]. The number of active functional groups in monomers [28] plays an important role in photopolymerization reactions. Compared to monomers with single-function group, those with multi-function group can significantly increase the density of crosslinking, and improve the strength and hardness of printed green bodies. However, the increasing number of functional groups also leads to increased viscosity of the slurry, which is not conducive to 3D printing. Refractive index matching [29, 30] is another factor in the selection of monomers. According to Lambert Beer's law, the curing depth is inversely proportional to the square of the refractive index difference between photosensitive resin and ceramic particles. Therefore, when the refractive index of monomers approaches that of ceramic particles, it can effectively limit scattering effects and increase curing depth, thereby improving the printing success rate. In addition, the curing performance of monomers and the thermal decomposition of the cured products are also important factors to facilitate the later degreasing process [31]. Overall, the selection of monomers directly affects the printing performance of photosensitive resins, as well as the properties and surface quality of the cured resin blocks, which further has a key impact on the structure and properties of 3D printed ceramic materials.

In this work, alumina ceramics for armor protection were manufactured by DLP 3D printing, before which photosensitive resins with different monomers, i.e., dipropylene glycol diacrylate (DPGDA), 16-hexanediol diacrylate (HDDA), trimethylolpropane triacrylate (TMPTA) were prepared. The influence of monomer type on the 3D printing performance of the slurry was conducted to explore the optimal formula of photosensitive resin. The microstructures and properties of 3D printed alumina ceramics were investigated.

2. Materials and Methods

2.1 Photosensitive slurry

In the photosensitive resin, the oligomer employed in this work was polyurethane acrylate (PUA), the photoinitiator was TPO-L, and the effects of monomers on the photosensitive resin slurry were investigated using DPGDA, HDDA, and TMPTA as monomers, respectively. The oligomer and monomer were mixed in mass ratio of 1:1, and then 4 wt.% of photoinitiator (TPO-L) was added. The photosensitive resin premix was obatined after the mixture was stirred for 2 hours and then stood for 24 hours until the bubbles disappeared completely. The above organic materials are all analytical pure and purchased from Shanghai Yinchang New Materials Co., Ltd, China.

Alumina powders were added into the photosensitive resin premixure with solid loading of 56 vol.%, and stirred into uniformity via ball milling for 180 minutes. The alumina powders in purity of >99.99% were purchased from Sumitomo Co., Ltd, Japan, and

the particle size distribution in Fig. 1 showed a mean diameter of 4.0 μm. The photosensitive ceramic slurry was finally obtained after filtering and vacuum defoaming.

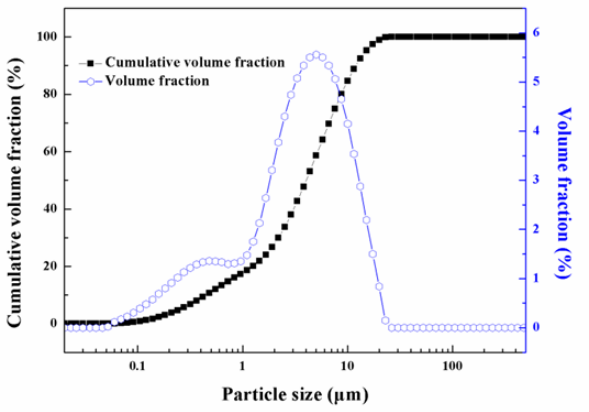

Fig. 1 Particle size distribution of the alumina powders

2.2 3D printing and sintering

The mixed ceramic slurry was poured into a DLP 3D printer (Autocera-M, Beijing Shiwei Technology), and layer by layer 3D printing was performed based on a pre-established digital model, as expressed by the diagrammatic sketch in Fig. 2.

After printing, the green body was washed in an ultrasonic cleaner to remove the excess slurry, and dried in a drying oven. The dried body was then placed in a muffle furnace for degreasing and sintering, during which the final sintering temperature was 1700 ℃ and held for 4 hours.

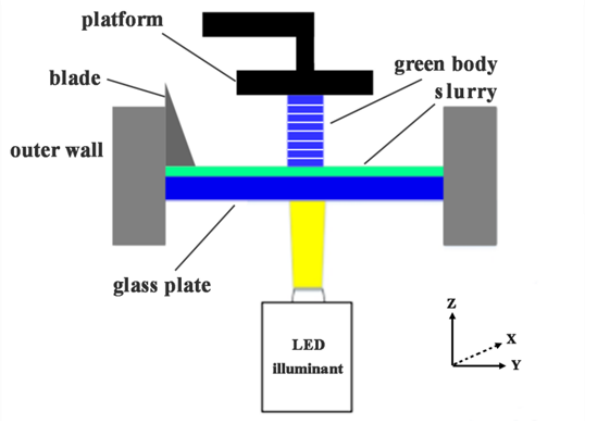

Fig. 2 Schematic diagram of DLP 3D printing process

2.3 Characterization and testing

The viscosity of photosensitive resin and ceramic slurry was measured in terms of a constant temperature viscometer (THS-NDJ-5S, Shenzhen, China), with the rotor speed of 50r/min at 25 ℃. The dimensions of 3D printed green body was measured using a vernier calipers with a accuracy of 0.02 mm, and the volume shrinkage in photopolymerization was determined in comparison to the digital model of 55 mm×10 mm×4 mm.

The thickness of the curing layer was evaluated using a spiral micrometer after exposure and removal of uncured photosensitive resin. The measurement was carried out taking average value on the center point and four corner positions of the square cured film.

The critical exposure and critical transmission depth of the photosensitive resins with different monomers were determined based on Bear Lambert theorem [32, 33]:

$$C_d = D_P \ln\left(E_i/E_c\right), \quad (1)$$

Where C_d is the thickness of the curing layer by photopolymerization, i.e., the thickness measured by curing a photosensitive resin at a certain exposure energy density. D_p is the critical transmission depth, i.e., depth of light penetration that triggers the critical exposure energy required for photopolymerization. E_c is the critical exposure energy, below which the exposure energy is not able to make the photosensitive resin cured. E_i is the energy of the input light source on the resin surface depends on the optical machine power W_0 and exposure time t:

$$E_i = W_0 \times t, \quad (2)$$

The curing thickness of resin slurry was measured under different input energy, and fitted versus $\ln E_i$, and the value of D_p and E_c can be determined according to the slope and intercept values.

The thermogravimetric curve (TG) and differential thermogravimetric curve (DTG) of the 3D printed green body were measured using a thermal analyzer (TG209F1, NETZSCH, German) with heating rate of 5 ℃/min.

Scanning electron microscopy (SEM, JSM-5600LV, JEOL, Japan) was performed to analyze the microstructure of 3D printed samples before and after sintering. Archimedes' method was carried out to obation the bulk density and apparent porosity of the 3D printed ceramics samples after sintering according to ASTM C373 .

The room-temperature bending strength of sintered ceramic specimens was measured using an electronic universal testing machine (Instron5500R, USA) via the three-point bending method with loading speed of 1 mm/min. The specimen was a cuboid in scale of 40 mm×3 mm×2 mm, with span of 15 mm. Vickers hardness (HV) was measured by a microhardness machine (HXD-1000TM, Shanghai, China) with a load of 9.8 N and a holding time of 10 s. The fracture toughness (KIC) was measured by the single-edge notched beam method (SENB) with loading speed of 0.1 mm/min, span of 20 mm, using test bars of 30 mm×6 mm×4 mm with notch depth of 2.5 mm. Each value of the properties was based on the average of no less than 5 specimens.

A split Hopkinson pressure bar test (SHPB) was performed on the alumina ceramics after sintering, to reveal their dynamic mechanical properties. The stress wave spreading along the SHPB was recorded, and the load and displacement of the pressure bar were plotted as function of time, after which the dynamic stress-strain curves were obatined for the samples.

3. Results and discussion

3.1. Properties of resins and slurries

The viscosities of photosensitive resins and ceramic slurries with different monomers was shown in Fig. 3 The photosensitive resin and ceramic slurry showed the lowest viscosity of 360 mPa·s and 1620 mPa·s as HDDA was employed as monomer; meanwhile, the viscosity showed largest values of up to 2910 mPa·s and 6540 mPa·s, with the monomer of DPGDA and TMPTA. It is noted that, TMPTA is an active agent with three functional groups and owns the highest molar mass; therefore, the photosensitive resin with the monomer of TMPTA showed higher viscosity than others. Both HDDA and DPGDA have two functional groups, and the molecular weight of DPGDA (242) is slightly larger than that of HDDA (224); therefore, the photosensitive resin and slurry with monomer of HDDA showed the most significant dilution effect and lowest viscosity.

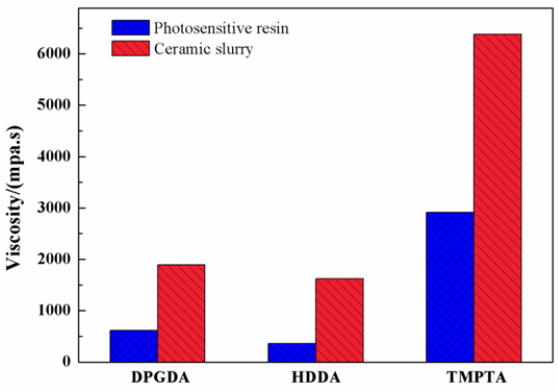

Fig. 3 The viscosities of photosensitive resins and ceramic slurries with different monomers.

Fig. 4 showed the effect of monomer types on the volume shrinkage during UV curing of photosensitive resins and ceramic slurries. It was suggested that, the volume shrinkage of photosensitive resin and ceramic slurries reached the maximum values of 4.36% and 1.43%, respectively, when TMPTA was employed as the monomer. Meanwhile, the minimum values of 1.72% and 0.46% were shown when DPGDA was used as the monomer. It is noted that, the monomer of TMPTA with three functional groups has higher numbers and densities of double bonds than HDDA and DPGDA with two functional groups. In the process of UV curing, larger quantities of crosslinking points were generated, and more molecular bonding transforms from van der Waals bonds into covalent bonds, resulting in a larger volume shrinkage. Although both HDDA and DPGDA have two functional groups, due to their smaller molecular weight of HDDA, it exhibited better molecular fluidity during curing under a certain exposure energy, which resulted in a higher volume shrinkage.

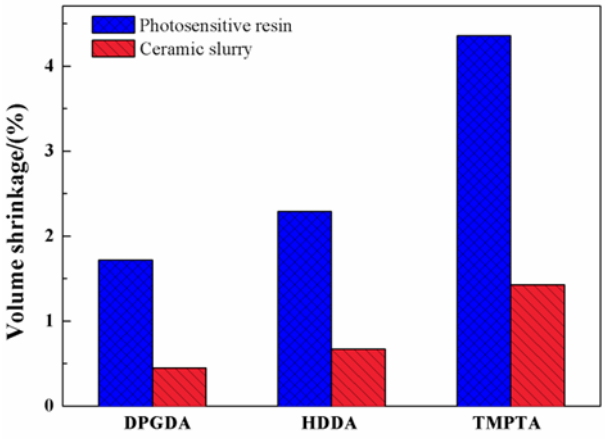

Fig. 4 The volume shrinkages of photosensitive resins and ceramic slurries with different monomers during UV curing.

The curing thickness of photosensitive resin as function of different monomers were measured under certain exposure energy densities, as listed in Table 1. For each monomer with whether two or three functional groups, the curing thickness showed monotonic increase with increasing exposure energy density. As the exposure energy density was 150 mJ/cm^2, the values of curing thickness were 0.56 mm, 0.68 mm and 0.85 mm for photosensitive resins with monomers of HDDA, DPGDA and TMPTA, respectively.

The curing thickness (Cd) was plotted versus the natural logarithm of exposure energy (lnE), and the linear fitting was performed and displayed in Fig. 5(a). It was shown that, the slope of the fitting line of the TMPTA photosensitive resin system was much larger than those of the other two monomers, and the fitting lines of HDDA and DPGDA photosensitive resins were nearly parallel with similar slopes. The critical transmission

depth and critical exposure energy were determined based on the slope and intercept of the fitting line, as plotted in Fig. 5(b). It was shown that, the critical exposureenergy of photosensitive resins with monomers of DPGDA, HDDA, and TMPTA were 17.7, 22.8, and 27.5 mJ/cm^2, respectively, and the critical transmission depths were 0.31, 0.30, and 0.48mm. Generally speaking, the smaller critical exposure energy make it easier for the photosensitive resin to transform into bulks by UV curing under a certain energy [34] Therefore, the monomer of TMPTA with three functional groups made the curing of photosensitive resin most difficult, while DPGDA made that easiest.

Table 1 Curing thickness (mm) of photosensitive resin with different monomer under certain exposure energy (mJ/cm^2)

E / Cp / Monomer	30	45	60	75	90	105	120	135	150
DPGDA	0.15	0.3	0.4	0.44	0.5	0.53	0.6	0.61	0.68
HDDA	0.1	0.15	0.31	0.37	0.44	0.47	0.49	0.54	0.56
TMPTA	0.11	0.16	0.37	0.48	0.56	0.69	0.69	0.78	0.85

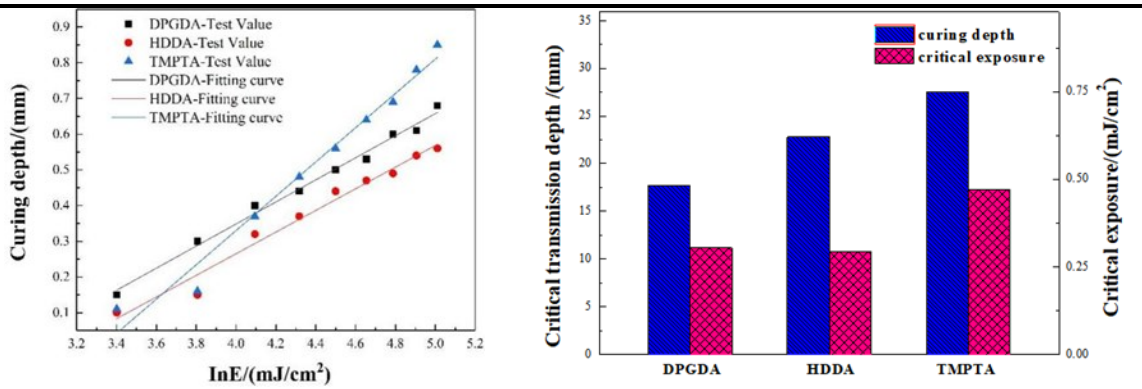

(**a**) (**b**)

Fig. 5 (a) The curing thickness plotted versus lnE along with the linear fitting; (b) the critical transmission depth and critical exposure energy of the photosensitive resins with different monomers.

3.2 Sintering procedure

TG-DTG curves of the 3D printed green body were plotted in Fig. 6 (a). It is shown that, the green body exhibited significant mass loss at 262 ℃, 365 ℃, and 505 ℃, respectively. After 600 ℃, the TG curve tends to stable, suggesting complete thermal decomposition of the organic resins, and the mass loss was about 25 wt.%. Therefore, the detailed sintering procedure of the ceramics was determined based on the TG curve, and shown in Fig.6(b). During sintering, appropriate holding for 1 hour at 262 ℃, 365 ℃, and 505 ℃ is demanded to ensure fully elimination of the organic resin without damaging the ceramic bodies. After the degreasing process is completed, the sample underwent a quick heating to 1200 ℃ along with a short holding, after which the sample was further heated to 1700 ℃ and held for 4 hours.

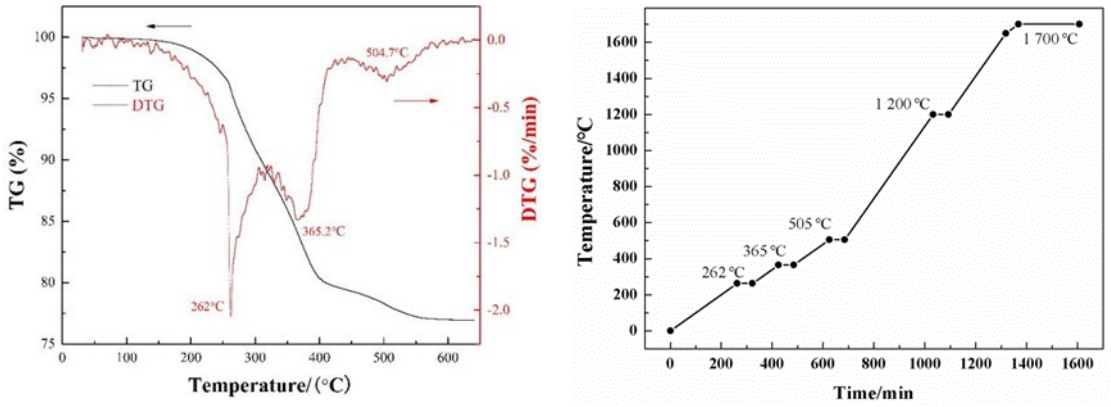

(**a**) (**b**)

Fig. 6 (a) TG-DTG curves of the 3D printed green body; (b) the detailed sintering procedure of ceramics.

3.3 Microstructure of the ceramics

Fig. 7 showed the SEM images of the green bodies 3D printed with different monomers. When DPGDA is employed as monomer, the 3D printed green body showed uniform microstructures with tiny interlayer cracks in Fig. 7(a). The sample using HDDA as monomer showed an anisotropic microstructure with thin parallel cracks between the printing layers (Fig. 7b). In the sample with monomer of TMPTA, the microstructure got rougher, and the gaps between the printing layers deteriorated seriously with width of up to 40 μm (Fig. 7c). Similar anisotropic microstructure with interlayer gaps have been reported in various literatures[35-37]. According to Fig. 5, the monomer of TMPTA with three functional groups made the curing of photosensitive resin most difficult, and some photosensitive resins remain uncured and transform into interlayer gaps in the body. Therefore, the gap between the printing layers was deteriorated in 3D printing of photosensitive resins with TMPTA.

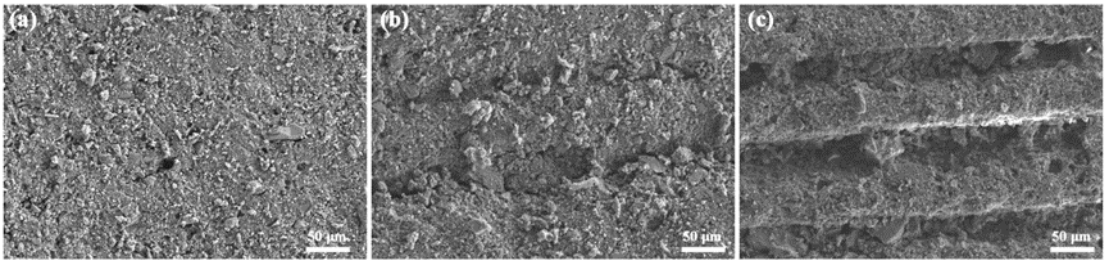

Fig. 7 SEM images of the green bodies 3D printed with different monomers: (a) DPGDA; (b) HDDA; (c) TMPTA

Fig. 8 shows the SEM images of the sintered samples 3D printed with different monomers. After sintering, the cracks disappeared completely when DPGDA and HDDA are employed as monomers in Fig. 8(a,b). It is confirmed that, the particles re-arrangement between different printing layers took place during sintering, which discharged the directional arranged pores in the interlayer ares. Therefore, the microstructures turned to be dense and uniform without anisotropic features. In the sample with TMPTA (Fig. 8c), the gaps between the printing layers are still serious, even though narrowing significantly during sintering. It is suggested that, the sintering driving force was unable to discharge the large interlayer gaps, as the width was up to 40 μm in the green body.

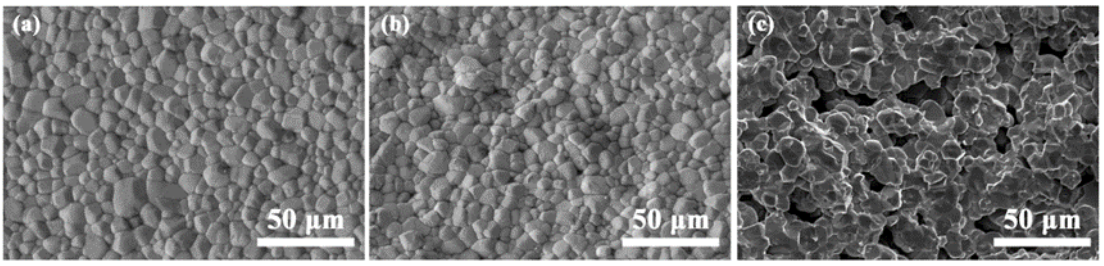

Fig. 8 SEM images of the sintered samples 3D printed with different monomers: (a) DPGDA; (b) HDDA; (c) TMPTA

Table 2 Properties of the alumina ceramics with different monomers

Monomer	Relative density (%)	Grain size (μm)	Hv (GPa)	KIC (MPa·m$^{1/2}$)	σ(MPa)
DPGDA	97.5	15.9	19.8±1.6	2.6±0.27	690±54
HDDA	96.7	15.7	19.1±2.3	2.4±0.35	660±76
TMPTA	90.2	16.9	15.7±4.1	1.9±0.52	510±76

Deatiled properties of the 3D printed ceramics with different monomers after sintering were measured and listed in table 2. Based on Archimedes method, the relative densities were 97.5% and 96.7%, for the ceramics with monomers of DPGDA and HDDA, respectively, and these values were in agreement with the dense microstructures in SEM images (Fig. 8a,b). As the monomer was TMPTA, the relative density was as low as 90.2%, which was attributed to the residual gaps between the printing layers in Fig. 8(c). Regardless of the monomers, the samples showed similar grain size of about 16 μm. As listed in Table 2, the alumina ceramics with monomer of DPGDA showed optimal mechanical properties with Vickers hardness of 19.8±1.6 GPa, fracture toughness of 2.6±0.27 MPa·m$^{1/2}$, and bending strength of 690±54 MPa. The sample with TMPTA showed deteriorated mechanical properties, due to the low relative density and serious interlayer gaps.

A SHPB test was conducted to investigate the dynamic mechanical properties of the alumina ceramics after sintering. The strain rate of SHPB test was 1200 s^{-1}, and the obatined dynamic stress-strain curves were displayed in Fig. 9. Regardless of the monomers, the alumina ceramics showed an near-linear deformation of about 3% before the maximum stress, which was regarded as elastic deformation and became major mode of the deformation. After the elastic deformation, a nonlinear deformation with strength reduction was exhibited, which was attibuted to the spreading of main cracks in a loading with high strain rates. The stress-strain curves in this work displayed typical features of brittle alumina ceramics, as the nonlinear deformation after maximum stress is unrelated to plastic deformation, even though the total strain was up to 6%. Compared to the static mechanical tests, the values of maximum stress and strain were very high in dynamic tests with high strain rates. Considering that the major mechanism of deformation in brittle material including ceramics is the propagation of cracks [38, 39], in dynamic mechanical tests, the speed of crack spreading was much lower than the loading rate, and it was impossible for the cracks to spread in time. The delay of crack spreading leaded to belated sample fracture, achieving higher strength and strain values for the alumina ceramics at higher strain rates. For the alumina ceramics with different monomers, the sample with DPGDA showed supeiror performance with dynamic strength of 3.7 GPa due to the dense and uniform microstructure in in Fig. 8(a), which was beneficial to the application in ar-

mor protection. In comparison, the sample with TMPTA showed worst dynamic performance with dynamic strength of 2.5 GPa, attributed to the inhomogeneous microstructure with interlayer gaps and numerous pores in in Fig. 8(c). It was suggested that, the pores acted as crack source and the interlayer gaps provided easy path for crack spreading, which cooperately deteriorated the dynamic mechanical property of alumina ceramics.

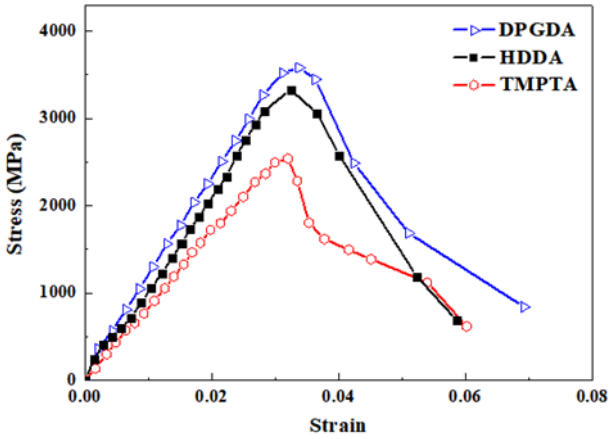

Fig. 9 Dynamic stress-strain curves of the sintered alumina ceramics by 3D printing with different monomers: (a) DPGDA; (b) HDDA; (c) TMPTA

4. Conclusions

In this work, alumina ceramics for armor protection were manufactured by 3D printing, and the effects of different monomers, i.e., DPGDA, HDDA, and TMPTA on the performance of the photosensitive slurry and microstructures and properties of 3D printed alumina ceramics were investigated. The conclusions are as follows:

(1) The photosensitive slurries using DPGDA as monomers with solid loading of 56 vol.% displayed optimal curing performance with low viscosity of 2910 mPa·s and small volume shrinkage of 0.46% in 3D printing, and the photosensitive resin with monomer of DPGDA showed the lowest critical exposure energy of 27.5 mJ/cm^2 suggesting easy curing into bulks. Each of the above properties was conducive to the curing performance in 3D printing, making it a suitable formula for 3D printing of ceramic materials.

(2) In the 3D printed sample using DPGDA as monomer, uniform microstructures with tiny cracks were exhibited in the green body, and the cracks disappeared completely after sintering due to the particle re-arrangement between different printing layers, resulting in dense and uniform microstructure without anisotropic features. In comparison, when TMPTA was employed as monomer, the green body showed anisotropic microstructure with serious interlayer gaps in width of up to 40 μm, which was attributed to the difficult curing of TMPTA with three functional groups. Furthermore, the sintering driving force was unable to discharge the wide interlayer gaps, making inhomogeneous microstructure with residual interlayer gaps and numerous pores.

(3) The different monomers further had significant effect on the mechanical properties of alumina ceramics after sintering. The sample with monomer of TMPTA showed poor mechanical properties, attributed to the low relative density and serious interlayer gaps in the microstructure. In comparion, the dense uniform microstructure in the sample with DPGDA as monomer contributed to superior mechanical properties, with Vickers hardness of 19.8±1.6 GPa, fracture toughness of 2.6±0.27 MPa·m$^{1/2}$, bending strength of 690±54 MPa, and dynamic strength of 3.7 GPa at strain rate of 1200 s^{-1}, which was beneficial to the application in armor protection.

Author Contributions: Conceptualization, D.Z. and X.X.; methodology, D.Z., X.C. and X.P.; investigation, X.C., Z.C. and X.G; resources, X.G; writing—original draft preparation, D.Z.; writing—review and editing, Z.C. and X.X.; supervision, Z.C. and X.X.; funding acquisition, X.X. All authors have read and agreed to the published version of the manuscript.

Funding: This research was funded by the Key Research and Development Project of Shaanxi Province of China, grant number 2024GX-YBXM-398

Institutional Review Board Statement: Not applicable

Informed Consent Statement: Not applicable

Data Availability Statement: Not applicable

Conflicts of Interest: The authors declare no conflict of interest.

References

1. Zhang, P.; Zhou, F.; Zhang, C.; Yan, Z.; Li, J.; Jin, H.; Zhang, H.; Lu, J., Charge trapping characteristics of alumina based ceramics. *Ceramics International* **2018,** 44, (11), 12112-12117.

2. Nötzel, D.; Hanemann, T., New feedstock system for fused filament fabrication of sintered alumina parts. *Materials* **2020,** 13, (19), 4461.

3. Obikawa, T.; Matsumura, T.; Shirakashi, T.; Usui, E., Wear characteristic of alumina coated and alumina ceramic tools. *Journal of materials processing technology* **1997,** 63, (1-3), 211-216.

4. Wang, W.; Chen, J.; Sun, X.; Sun, G.; Liang, Y.; Bi, J., Influence of additives on microstructure and mechanical properties of alumina ceramics. *Materials* **2022,** 15, (8), 2956.

5. Tang, S.; Fu, L.; Gu, H.; Huang, A.; Yang, S.; Lv, R., Improved mechanical properties of alumina ceramics using plasma-assisted milling technique. *Materials* **2023,** 16, (3), 1128.

6. Golestani-fard, F.; Mazaheri, M.; Aminzare, M.; Ebadzadeh, T., Microstructural evolution of a commercial ultrafine alumina powder densified by different methods. *Journal of the European Ceramic Society* **2011,** 31, (14), 2593-2599.

7. Wang, L.; An, L.; Zhao, J.; Shimai, S.; Mao, X.; Zhang, J.; Liu, J.; Wang, S., High-strength porous alumina ceramics prepared from stable wet foams. *Journal of Advanced Ceramics* **2021,** 10, (4), 852-859.

8. Ropuš, I.; Ćurković, L.; Cajner, H.; Rončević, S., Optimization of alumina ceramics corrosion resistance in nitric acid. *Materials* **2022,** 15, (7), 2579.

9. Yanyuan, L.; Daming, C.; Jianfeng, T., Compression Dynamic Performance of Bulletproof Alumina Ceramic. *Rare Metal Materials and Engineering* **2013,** 42, 956-959.

10. Bilal, A.; Jahan, M. P.; Talamona, D.; Perveen, A., Electro-discharge machining of ceramics: A review. *Micromachines* **2018,** 10, (1), 10.

11. Heng, L.; Kim, J. S.; Song, J. H.; Mun, S. D., A review on surface finishing techniques for difficult-to-machine ceramics by non-conventional finishing processes. *Materials* **2022,** 15, (3), 1227.

12. Yu, A.; Tan, Y.; Yang, X., Machining characteristics of Ce-ZrO2/CePO4 ceramics. *JOURNAL OF RARE EARTHS* **2004,** 22, 223-225.

13. Eckel, Z. C.; Zhou, C.; Martin, J. H.; Jacobsen, A. J.; Carter, W. B.; Schaedler, T. A., Additive manufacturing of polymer-derived ceramics. *Science* **2016,** 351, (6268), 58-62.

14. Zocca, A.; Colombo, P.; Gomes, C. M.; Günster, J., Additive manufacturing of ceramics: issues, potentialities, and opportunities. *Journal of the American Ceramic Society* **2015,** 98, (7), 1983-2001.

15. Chen, Z.; Li, Z.; Li, J.; Liu, C.; Lao, C.; Fu, Y.; Liu, C.; Li, Y.; Wang, P.; He, Y., 3D printing of ceramics: A review. *Journal of the European Ceramic Society* **2019,** 39, (4), 661-687.

16. Li, H.; Liu, Y.; Liu, Y.; Zeng, Q.; Hu, K.; Lu, Z.; Liang, J.; Li, J., Influence of debinding holding time on mechanical properties of 3D-printed alumina ceramic cores. *Ceramics International* **2021,** 47, (4), 4884-4894.
17. Li, Q.; An, X.; Liang, J.; Liu, Y.; Hu, K.; Lu, Z.; Yue, X.; Li, J.; Zhou, Y.; Sun, X., Balancing flexural strength and porosity in DLP-3D printing Al_2O_3 cores for hollow turbine blades. *Journal of Materials Science & Technology* **2022,** 104, 19-32.
18. Wang, S.; Peng, L.; Song, C.; Wang, C., Digital light processing additive manufacturing of thin dental porcelain veneers. *Journal of the European Ceramic Society* **2023,** 43, (3), 1161-1167.
19. Li, H.; Hu, K.; Liu, Y.; Lu, Z.; Liang, J., Improved mechanical properties of silica ceramic cores prepared by 3D printing and sintering processes. *Scripta Materialia* **2021,** 194, 113665.
20. Zheng, W.; Wu, J.-M.; Chen, S.; Yu, K.-B.; Hua, S.-B.; Li, C.-H.; Zhang, J.-X.; Shi, Y.-S., Fabrication of high-performance silica-based ceramic cores through selective laser sintering combined with vacuum infiltration. *Additive Manufacturing* **2021,** 48, 102396.
21. Ma, C.; He, C.; Wang, W.; Yao, X.; Yan, L.; Hou, F.; Liu, J.; Guo, A., Metal-doped polymer-derived SiOC composites with inorganic metal salt as the metal source by digital light processing 3D printing. *Virtual and Physical Prototyping* **2020,** 15, (3), 294-306.
22. Fan, J.; Xu, X.; Niu, S.; Zhou, Y.; Li, X.; Guo, Y.; Luo, Y., Anisotropy management on microstructure and mechanical property in 3D printing of silica-based ceramic cores. *Journal of the European Ceramic Society* **2022,** 42, (10), 4388-4395.
23. Qian, C.; Hu, K.; Lu, Z.; Li, P., Volume shrinkage and conversion rate of Al_2O_3 ceramic stereolithography suspension polymerised by ultraviolet light. *Materials Chemistry and Physics* **2021,** 267, 124661.
24. Niu, S.; Luo, Y.; Li, X.; Chen, Y.; Cheng, Y.; Dai, S.; Zhang, Q.; Li, H.; Xu, X., 3D printing of silica-based ceramic cores reinforced by alumina with controlled anisotropy. *Journal of Alloys and Compounds* **2022,** 922, 166325.
25. Kim, I.; Kim, S.; Andreu, A.; Kim, J.-H.; Yoon, Y.-J., Influence of dispersant concentration toward enhancing printing precision and surface quality of vat photopolymerization 3D printed ceramics. *Additive Manufacturing* **2022,** 52, 102659.
26. Xu, X.; Zhou, S.; Wu, J.; Zhang, C.; Liu, X., Inter-particle interactions of alumina powders in UV-curable suspensions for DLP stereolithography and its effect on rheology, solid loading, and self-leveling behavior. *Journal of the European Ceramic Society* **2021,** 41, (4), 2763-2774.
27. Mu, Y.; Chen, J.; An, X.; Liang, J.; Li, J.; Zhou, Y.; Sun, X., Effect of synergism of solid loading and sintering temperature on microstructural evolution and mechanical properties of 60 vol% high solid loading ceramic core obtained through stereolithography 3D printing. *Journal of the European Ceramic Society* **2023,** 43, (2), 661-675.
28. Song, S. Y.; Park, M. S.; Lee, D.; Lee, J. W.; Yun, J. S., Optimization and characterization of high-viscosity ZrO2 ceramic nano-composite resins for supportless stereolithography. *Materials & Design* **2019,** 180, 107960.
29. Ozkan, B.; Sameni, F.; Bianchi, F.; Zarezadeh, H.; Karmel, S.; Engstrøm, D. S.; Sabet, E., 3D printing ceramic cores for investment casting of turbine blades, using LCD screen printers: The mixture design and characterisation. *Journal of the European Ceramic Society* **2022,** 42, (2), 658-671.
30. An, X.; Mu, Y.; Chen, J.; Liang, J.; Li, J.; Zhou, Y.; Sun, X., Compositional optimization of high-solid-loading ceramic cores via 3D printing. *Additive Manufacturing* **2022,** 58, 103054.
31. Li, H.; Liu, Y.; Liu, Y.; Zeng, Q.; Wang, J.; Hu, K.; Lu, Z.; Liang, J., Evolution of the microstructure and mechanical properties of stereolithography formed alumina cores sintered in vacuum. *Journal of the European Ceramic Society* **2020,** 40, (14), 4825-4836.
32. Gentry, S. P.; Halloran, J. W., Depth and width of cured lines in photopolymerizable ceramic suspensions. *Journal of the European Ceramic Society* **2013,** 33, (10), 1981-1988.
33. Zakeri, S.; Vippola, M.; Levänen, E., A comprehensive review of the photopolymerization of ceramic resins used in stereolithography, Addit. Manuf. 35 (2020) 101177. 2020.
34. Qian, C.; Hu, K.; Li, J.; Li, P.; Lu, Z., The effect of light scattering in stereolithography ceramic manufacturing. *Journal of the European Ceramic Society* **2021,** 41, (14), 7141-7154.

35. Wang, X.; Zhou, Y.; Zhou, L.; Xu, X.; Niu, S.; Li, X.; Chen, X., Microstructure and properties evolution of silicon-based ceramic cores fabricated by 3D printing with stair-stepping effect control. *Journal of the European Ceramic Society* **2021,** 41, (8), 4650-4657.
36. Li, Q.; Hou, W.; Liang, J.; Zhang, C.; Li, J.; Zhou, Y.; Sun, X., Controlling the anisotropy behaviour of 3D printed ceramic cores: From intralayer particle distribution to interlayer pore evolution. *Additive Manufacturing* **2022,** 58, 103055.
37. Li, H.; Liu, Y.; Colombo, P.; Li, W.; Liu, Y.; Hu, K.; Lu, Z., The influence of sintering procedure and porosity on the properties of 3D printed alumina ceramic cores. *Ceramics International* **2021,** 47, (19), 27668-27676.
38. Zhang, D.; Yu, R.; Feng, X.; Guo, X.; Yang, Y.; Xu, X., Enhanced Mechanical Properties of Al_2O_3 Nanoceramics via Low Temperature Spark Plasma Sintering of Amorphous Powders. *Materials* **2023,** 16, (16), 5652.
39. Appleby-Thomas, G. J.; Hazell, P., A study on the strength of an armour-grade aluminum under high strain-rate loading. *Journal of Applied Physics* **2010,** 107, (12), 123508 .